Article

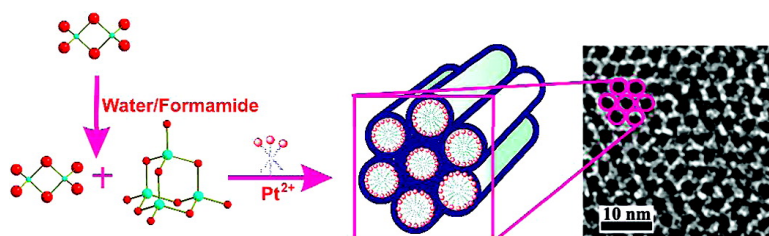# Importance of Solution Equilibria in the Directed Assembly of Metal Chalcogenide Mesostructures

Santanu Bag, and Mercouri G. Kanatzidis

More About This Article

Additional resources and features associated with this article are available within the HTML version:

- Supporting Information
- Links to the 1 articles that cite this article, as of the time of this article download
- Access to high resolution figures
- Links to articles and content related to this article
- Copyright permission to reproduce figures and/or text from this article

View the Full Text HTML

Importance of Solution Equilibria in the Directed Assembly of Metal Chalcogenide Mesostructures

Santanu Bag and Mercouri G. Kanatzidis*

Department of Chemistry, Northwestern University, Evanston, Illinois 60208

Received January 29, 2008; E-mail: m-kanatzidis@northwestern.edu

Abstract: We describe the new nanostructured Pt/Ge/Se materials prepared from the molecular units $[Ge_2Se_6]^{4-}$ and $[GeSe_4]^{4-}$ and linking Pt^{2+} ions in the presence of surfactant micelles. X-ray diffraction coupled with transmission electron microscopy images reveals hexagonal pore symmetry. The solvent dependence and solution speciation of these building blocks were investigated by means of multinuclear NMR spectroscopy and by fast atom bombardment (FAB) mass spectroscopy and it is shown that rapid exchange equilibrium is reached between species like $[Ge_4Se_{10}]^{4-}$, $[Ge_2Se_6]^{4-}$, and $[GeSe_4]^{4-}$ in both water and formamide. This results in multiple Ge/Se anions being incorporated in the mesostructured materials which is supported by Raman and IR spectroscopic data. It is likely that the presence of multiple building units both in water and formamide solutions favors the assembly of mesostructured metal chalcogenides with good pore order. Systematic variation of both surfactant headgroup and chain length modulates the optoelectronic properties of the mesostructures. The Pt/Ge/Se materials show sharp band gap transitions in the range of 1.24−1.97 eV. Finally, the materials exhibit reversible ion-exchange properties and a marked inorganic framework flexibility that enables a contraction−expansion process in response to the exchange. The Pt/Ge/Se framework possesses a very high surface area as estimated by small-angle X-ray scattering techniques.

Introduction

Mesoporous solids are open-framework materials with pores in the 2−50 nm size range. They are now some of the most actively studied materials because of their promise for applications in a wide variety of fields ranging from separations,[1–5] catalysis,[6] and host guest chemistry[7,8] to low-k dielectric coatings.[9] Though oxide-based materials have attracted most of the attention,[10,11] porous nonoxidic counterparts are emerging as a unique subclass[12] that offers the possibility to combine porosity and optoelectronic functionality in a single system promising new capabilities in sensing, photo- and electro-catalytic applications. Prominent members of this subclass are the chalcogenides and a number of elements.[13–17] To date,

mesoporous metal chalcogenides with accessible pores are scarce,[1,18,19] but materials with occupied pores are known and have band-gaps starting from ∼3 to less than 0.7 eV.[20–35] The synthesis of metal chalcogenide mesostructured materials involves supramolecular assembly of suitable anionic clusters around liquid crystal templates in the presence of appropriate linking metal ions. The solvent and temperature can strongly affect the overall pore order of the mesostructured materials.

Materials with mesopores have been reported using the chalcogenide building blocks $[SnSe_4]^{4-}$, $[Sn_2S_6]^{4-}$, $[Sn_2Se_6]^{4-}$, $[Ge_4S_{10}]^{4-}$, $[Ge_4Se_{10}]^{4-}$, $[Sn_4Se_{10}]^{4-}$, $[SnTe_4]^{4-}$, $[MoS_4]^{2-}$, and $[SbSe_4]^{3-}$ and different linking metal ions (Mn^{2+}, Fe^{2+}, Co^{2+}, Ni^{2+}, Zn^{2+}, Cd^{2+}, Hg^{2+}, Ga^{3+}, In^{3+}, Sb^{3+}, Sn^{4+}, Pt^{2+}, Pt^{4+},

(1) Bag, S.; Trikalitis, P. N.; Chupas, P. J.; Armatas, G. S.; Kanatzidis, M. G. *Science* **2007**, *317*, 490–493.
(2) Kisler, J. M.; Dahler, A.; Stevens, G. W.; O'Connor, A. J. *Microporous Mesoporous Mater.* **2001**, *44*, 769–774.
(3) Feng, X.; Fryxell, G. E.; Wang, L. Q.; Kim, A. Y.; Liu, J.; Kemner, K. M. *Science* **1997**, *276*, 923–926.
(4) Han, Y. J.; Stucky, G. D.; Butler, A. *J. Am. Chem. Soc.* **1999**, *121*, 9897–9898.
(5) Brown, J.; Mercier, L.; Pinnavaia, T. J. *Chem. Commun.* **1999**, *1*, 69–70.
(6) Climent, M. J.; Corma, A.; Iborra, S.; Miquel, S.; Primo, J.; Rey, F. *J. Catal.* **1999**, *183*, 76–82.
(7) Moller, K.; Bein, T. *Chem. Mater.* **1998**, *10*, 2950–2963.
(8) Yiu, H. H. P.; Wright, P. A.; Botting, N. P. *Microporous Mesoporous Mater.* **2001**, *44*, 763–768.
(9) Wang, Z. B.; Wang, H. T.; Mitra, A.; Huang, L. M.; Yan, Y. S. *Adv. Mater.* **2001**, *13*, 746–749.
(10) Kresge, C. T.; Leonowicz, M. E.; Roth, W. J.; Vartuli, J. C.; Beck, J. S. *Nature* **1992**, *359*, 710–712.
(11) Davis, M. E. *Nature* **2002**, *417*, 813–821.
(12) Kanatzidis, M. G. *Adv. Mater.* **2007**, *19*, 1165–1181.

(13) (a) Armatas, G. S.; Kanatzidis, M. G. *Science* **2006**, *313*, 817–820. (b) Armatas, G. S.; Kanatzidis, M. G. *Nature* **2006**, *441*, 1122–1125.
(14) Sun, D.; Riley, A. E.; Cadby, A. J.; Richman, E. K.; Korlann, S. D.; Tolbert, S. H. *Nature* **2006**, *441*, 1126–1130.
(15) Attard, G. S.; Bartlett, P. N.; Coleman, N. R. B.; Elliott, J. M.; Owen, J. R.; Wang, J. H. *Science* **1997**, *278*, 838–840.
(16) Attard, G. S.; Goltner, C. G.; Corker, J. M.; Henke, S.; Templer, R. H. *Angew. Chem., Int. Ed. Engl.* **1997**, *36*, 1315–1317.
(17) Johnson, S. A.; Ollivier, P. J.; Mallouk, T. E. *Science* **1999**, *283*, 963–965.
(18) Vanchura, B. A.; He, P. G.; Antochshuk, V.; Jaroniec, M.; Ferryman, A.; Barbash, D.; Fulghum, J. E.; Huang, S. D. *J. Am. Chem. Soc.* **2002**, *124*, 12090–12091.
(19) Mohanan, J. L.; Arachchige, I. U.; Brock, S. L. *Science* **2005**, *307*, 397–400.
(20) (a) Trikalitis, P. N.; Rangan, K. K.; Bakas, T.; Kanatzidis, M. G. *Nature* **2001**, *410*, 671–675. (b) Rangan, K. K.; Billinge, S. J. L.; Petkov, V.; Heising, J.; Kanatzidis, M. G. *Chem. Mater.* **1999**, *11*, 2629–2632.
(21) Trikalitis, P. N.; Bakas, T.; Papaefthymiou, V.; Kanatzidis, M. G. *Angew. Chem., Int. Ed.* **2000**, *39*, 4558–4562.
(22) Rangan, K. K.; Trikalitis, P. N.; Kanatzidis, M. G. *J. Am. Chem. Soc.* **2000**, *122*, 10230–10231.

Pd^{2+}).[20–36] Among these metals, Pt^{2+} has yielded materials of high pore order presumably because of its slower ligand substitution kinetics during the linking reaction that allows the structure more time to organize. Although the adamantane [Ge$_4$Se$_{10}$]$^{4-}$ cluster and various linking metals resulted in high quality mesostructured materials,[24] the corresponding dimeric [Ge$_2$Se$_6$]$^{4-}$ and monomeric [GeSe$_4$]$^{4-}$ species have not been studied. We will show here that unlike the adamantane these two species undergo transformation equilibria that complicate the assembly process.

We describe the synthesis of platinum-based hexagonal mesostructured systems from [Ge$_2$Se$_6$]$^{4-}$ and the [GeSe$_4$]$^{4-}$ clusters and explore the role of solution equilibria in controlling mesophase composition and pore organization. We find that systematic variation of surfactants changes the pore size and pore-pore spacing, the overall symmetry and even the energy band gaps of the mesostructured materials. Surprisingly, compared to the materials with cubic pore $Ia\bar{3}d$ symmetry obtained with the corresponding [Sn$_2$Se$_6$]$^{4-}$/Pt^{2+} combination,[26] the analogous [Ge$_2$Se$_6$]$^{4-}$ did not produce cubic pore symmetry. ^{77}Se NMR spectroscopy of [Ge$_2$Se$_6$]$^{4-}$, in water and formamide (FM) as well as fast atom bombardment mass spectroscopy (FABS) show multiple species present in equilibrium all of which can be incorporated into the Pt–Ge–Se framework. This is in contrast to the [Sn$_2$Se$_6$]$^{4-}$ system which shows only a single species. The implications of multiple building unit participation to assemble hexagonally ordered materials is discussed. The new materials described here exhibit reversible ion-exchange properties and flexible inorganic networks. Small angle X-ray scattering (SAXS) experiments on selected systems suggest a very high mesoporous surface for the inorganic framework.

Experimental Section

Starting Materials. K$_4$Ge$_2$Se$_6$ and K$_4$GeSe$_4$ were prepared according to a literature procedure.[37,38] K$_2$PtCl$_4$ was purchased from Strem Chemical Inc. Cetylpyridinium bromide monohydrate (C$_{16}$PyBr.H$_2$O) and formamide (FM) were purchased from Aldrich. The surfactants C$_n$H$_{2n+1}$N(C$_5$H$_5$)Br (denoted as C$_n$PyBr; n = 14, 18, and 20), C$_n$H$_{2n+1}$N(CH$_3$)$_2$(CH$_2$)$_3$N(CH$_3$)$_2$Br (denoted as C$_n$T-MPDABr; n = 20, 22), and C$_n$H$_{2n+1}$N(CH$_3$)$_2$(CH$_2$)$_2$N(CH$_3$)$_2$Br

(23) Rangan, K. K.; Trikalitis, P. N.; Bakas, T.; Kanatzidis, M. G. *Chem. Commun.* **2001**, *9*, 809–810.
(24) Trikalitis, P. N.; Rangan, K. K.; Kanatzidis, M. G. *J. Am. Chem. Soc.* **2002**, *124*, 2604–2613.
(25) Rangan, K. K.; Trikalitis, P. N.; Canlas, C.; Bakas, T.; Weliky, D. P.; Kanatzidis, M. G. *Nano Lett.* **2002**, *2*, 513–517.
(26) Trikalitis, P. N.; Rangan, K. K.; Bakas, T.; Kanatzidis, M. G. *J. Am. Chem. Soc.* **2002**, *124*, 12255–12260.
(27) Trikalitis, P. N.; Ding, N.; Malliakas, C.; Billinge, S. J. L.; Kanatzidis, M. G. *J. Am. Chem. Soc.* **2004**, *126*, 15326–15327.
(28) Trikalitis, P. N.; Bakas, T.; Kanatzidis, M. G. *J. Am. Chem. Soc.* **2005**, *127*, 3910–3920.
(29) Trikalitis, P. N.; Kerr, T. A.; Kanatzidis, M. G. *Microporous Mesoporous Mater.* **2006**, *88*, 187–190.
(30) Ding, N.; Takabayashi, Y.; Solari, P. L.; Prassides, K.; Pcionek, R. J.; Kanatzidis, M. G. *Chem. Mater.* **2006**, *18*, 4690–4699.
(31) MacLachlan, M. J.; Coombs, N.; Ozin, G. A. *Nature* **1999**, *397*, 681–684.
(32) MacLachlan, M. J.; Coombs, N.; Bedard, R. L.; White, S.; Thompson, L. K.; Ozin, G. A. *J. Am. Chem. Soc.* **1999**, *121*, 12005–12017.
(33) Riley, A. E.; Tolbert, S. H. *J. Am. Chem. Soc.* **2003**, *125*, 4551–4559.
(34) Korlann, S. D.; Riley, A. E.; Kirsch, B. L.; Mun, B. S.; Tolbert, S. H. *J. Am. Chem. Soc.* **2005**, *127*, 12516–12527.
(35) Riley, A. E.; Korlann, S. D.; Richman, E. K.; Tolbert, S. H. *Angew. Chem., Int. Ed.* **2006**, *45*, 235–241.
(36) Trikalitis, P.; Rangan, K. K.; Kanatzidis, M. G. *Mater. Res. Soc. Symp. Proc.* **2002**, *703*, 1–6.
(37) Eisenmann, B.; Hansa, J. *Z. Kristallogr.* **1993**, *203*, 301–302.
(38) Klepp, K. O. *Z. Naturforsch., B: Chem. Sci.* **1985**, *40*, 878–882.

(denoted as C$_n$TMEDABr; n = 20, 22) were synthesized by refluxing the corresponding alkyl-bromide with an excess of pyridine, N,N,N',N'-tetramethyl-1,3-propanediamine (denoted as TMPDA) and N,N,N',N'-tetramethyl-1,2-ethanediamine (denoted as TMEDA), respectively, in either ethanol or acetone. The solvent was removed using a rotary evaporator and pure compounds were obtained in high yield (>90%) after a single recrystallization from CHCl$_3$-ethyl acetate. Surfactant purity was checked by ^{1}H NMR after dissolving the solid sample in CDCl$_3$. The materials we describe here are generically formulated as *Surf*_Pt_Ge$_2$Se$_6$ and *Surf*_Pt_GeSe$_4$ and more specifically as C$_n$PyPt_Ge$_2$Se$_6$ or C$_n$TMPDAPt_Ge$_2$Se$_6$ or C$_n$TMEDAPt_Ge$_2$Se$_6$ or C$_n$PyPt_GeSe$_4$ based on the type of surfactants and starting building units used.

Mesostructured Platinum Germanium Selenides. All reactions were carried out inside a glovebox under nitrogen. In a typical preparation, 0.4 g of surfactant (for pyridinium based) was dissolved in 8 mL of FM under stirring. In another vial, 0.078 g (0.1 mmol) of K$_4$Ge$_2$Se$_6$ was dissolved in 1 mL of hot FM forming a clear deep yellow solution. An amount of 0.042 g (0.1 mmol) of K$_2$PtCl$_4$ was dissolved in another 1 mL of FM to make a deep orange-red solution. These two solutions were added dropwise at the same time to the surfactant solution over a period of 10 min using pipets. A dark brown-red solid formed within a few minutes and the mixture was stirred overnight at 75 °C. The dark pinkish brown product was isolated by filtration, washed with copious amount of warm (75 °C) FM and H$_2$O, and dried under vacuum (overall yield ~ 90% based on K$_4$Ge$_2$Se$_6$). For the other surfactants, 0.25 g was dissolved in 4 mL of hot FM and 0.15 mmol platinum salt was added instead of 0.1 mmol.

Synthesis of mesostructured C$_{16}$PyPt_Ge$_2$Se$_6$ in water was carried out using the same procedure as above, except 0.4 g of surfactant C$_{16}$PyBr.H$_2$O was dissolved in 4 mL of water (overall yield ~90% based on K$_4$Ge$_2$Se$_6$). However, slight variation of surfactant concentration did not affect the overall pore order of the final mesostructures.

In the case of [GeSe$_4$]$^{4-}$, 0.05 g of K$_4$GeSe$_4$ (0.1 mmol) and 0.4 g of surfactant was dissolved in 1 and 4 mL of hot FM respectively. An amount of 0.04 g (0.1 mmol) of K$_2$PtCl$_4$ dissolved in 1 mL of FM was added at the same time with K$_4$GeSe$_4$ solution to the surfactant solution. A dark brown precipitate was collected after aging overnight at 75 °C followed by washing with 30 mL each of hot FM and water with overall yield of ~75% based on K$_4$GeSe$_4$. The C$_n$PyPt_Ge$_2$Se$_6$ materials are stable in air for a couple of days, while those prepared from [GeSe$_4$]$^{4-}$ are stable only for couple of hours after which the pore structure collapsed.

Ion-Exchange Experiments. Ion exchange reactions were carried out in nitrogen atmosphere at 75 °C in FM. Typically, 1.2 g of C$_n$PyBr (e.g., n = 12) surfactant was dissolved in 6 mL of hot FM and then 0.15 g of mesostructured C$_{18}$PyPt_Ge$_2$Se$_6$ was added to it. The mixture was stirred for 22 h, filtered hot, washed subsequently with hot FM and water and then dried under vacuum. Ion exchange with smaller cationic species such as NH$_4^+$ was performed in a similar fashion as above using 0.12 g of CH$_3$COONH$_4$ dissolved in 12 mL of ethanol and adding 0.208 g of mesostructured C$_{18}$PyPt_Ge$_2$Se$_6$ material at room temperature. The NH$_4^+$ exchanged material is denoted as (NH$_4$)Pt_Ge$_2$Se$_6$.

Synthesis of Hexagonal Mesostructured Pt/Ge/Se Materials Using a Mixture of Selenogermanate Anions. An amount of 0.4 g of surfactant (C$_n$PyBr; n = 16, 18) was dissolved in 8 mL of FM under stirring. In another vial, 0.025 g (0.05 mmol) of K$_4$GeSe$_4$ and 0.07 g (0.05 mmol) of (TMA)$_4$Ge$_4$Se$_{10}$ were dissolved together in 1 mL of hot formamide. An amount of 0.042 g (0.1 mmol) of K$_2$PtCl$_4$ was dissolved in another 1 mL of FM to make a deep orange-red solution. These two solutions were added dropwise at the same time to the surfactant solution over a period of 10 min using pipets. A dark brown-red solid formed within a few minutes and the mixture was stirred overnight at 75 °C. The dark pinkish brown product was isolated by filtration, washed with copious amount of warm (75 °C) FM and H$_2$O, and dried under

vacuum. The powder X-ray diffraction of the product indicate a hexagonal order similar to the other hexagonal materials described here.

Physical Measurements. Powder X-ray Diffraction (XRD), Elemental Analysis, Thermogravimetric Analysis (TGA) and Mass Spectroscopy. Powder X-ray diffraction patterns were acquired on a Rigaku Rotaflex diffractometer (45 kV, 100 mA) using a rotating anode Cu Kα rotation source. The scan rates were 0.15 deg/min and a step size of 0.02 deg. Quantitative microprobe analyses were performed on a JEOL JSM-6400 V scanning electron microscope equipped with a Noran energy dispersive spectroscopy (EDS) detector. Data acquisition was performed with an accelerating voltage of 25 kV and 60 s accumulation time. Elemental C, H, N analyses were obtained on a Perkin-Elmer Series II CHNS/O Analyzer 2400. Thermogravimetric analyses were performed using a computer controlled Shimadzu TGA-50 analyzer. Typically, 40 mg of sample was placed in a silica bucket and heated in a nitrogen flow of 50 mL/min with a rate of 10 °C/min. Pyrolysis mass spectra were obtained with a TRIO-1 mass spectrometer. Samples were heated at 20 °C/min and the volatile products were ionized by electron ionization. A fast atom bombardment (FAB) mass spectrum was acquired using JEOL JMS HX 110 double focusing magnetic sector mass spectrometer and p-nitrobenzyl alcohol (NBA) was used as matrix.

Band Gap Measurements. UV/vis/near-IR diffuse reflectance spectra were obtained at room temperature on a Shimadzu UV-3010 PC double beam, double monochromator spectrophotometer in the wavelength range of 200−2500 nm. $BaSO_4$ powder was used as a reference (100% reflectance) and base material on which the powder sample was coated. The reflectance data were converted to absorption using the Kubelka-Munck function, and the band edge for each sample was estimated from the intercept of the line extrapolated from the high-energy end of the absorption to the baseline.[39]

Infrared and Raman Spectroscopic Measurements. Spectra in the far-infrared (Far-IR) region (600−100 cm^{-1}) were recorded with a computer-controlled Nicolet 750 Magna-IR series II spectrometer equipped with a TGS/PE detector and silicon beam splitter in 2 cm^{-1} resolution. Samples were diluted by making CsI pellets and then spectra were recorded in transmittance mode under inert nitrogen atmosphere. Raman spectra (3500−100 cm^{-1}) were recorded on a computer-controlled BIO-RAD Fourier transform FT-Raman spectrometer with a Spectra-Physics Topaz T10−106c 1064-nm YAG laser. The instrument was configured in 180° backscattering mode and samples were loaded into melting point capillary tubes.

Transmission Electron Microscopy (TEM). Transmission electron micrographs were obtained with a JEOL 2200FS instrument (field emission) operating at 200 kV using the facilities of the Center of Advanced Microscopy at Michigan State University. TEM samples were prepared by suspending the precipitate in diethyl ether, then casting on a holey carbon grid after 10 min of sonication.

Nuclear Magnetic Resonance (NMR) Spectroscopy. All ^{77}Se NMR spectra were recorded on a Varian UnityPlus-500 NMR spectrometer equipped with a 5-mm broadband probe over the frequency range 50−220 MHz and were obtained without locking. The spectrometer frequency was 95.367 MHz for ^{77}Se. Typical measurement conditions were a spectral width of 39024.4 Hz, a 90° pulse angle, an acquisition time of 0.5 s with data point resolution of 1.0 Hz/pt and 0.2 s relaxation delay between scans. The pulse width setting was 6.0 μs. An exponential multiplication of free induction decay of 5 Hz was used.

The ^{77}Se two-dimensional exchange spectroscopy (2D-EXSY) homonuclear exchange spectra were obtained at 65 °C. The pulse sequence for the 2D spectra was standard nuclear Overhauser

enhancement spectroscopy (NOESY) parameters.[40–42] The spectral width in both dimensions was 39024.4 Hz. The acquisition time was 0.21 s, and a relaxation delay of 0.5 s was used between transients. A total of 92 transients were collected for each of the 400 longitudinal relaxation time (t_1) increments. The mixing time (t_m) employed was 0.15 s. The F_1 dimension was zero-filled to 16384 points, a Gaussian function was applied to both dimension prior to Fourier transformation. A 3-fold linear prediction in the F_1 dimension was employed. The ^{77}Se nucleus was externally referenced to a sample of neat $(CH_3)_2$Se at 25 °C.

Solution ^{119}Sn NMR spectra were obtained without locking on Varian Inova 400 NMR spectrometer equipped with a 5-mm broadband probe. The spectrometer frequency was 149.341 MHz for ^{119}Sn. Typical measurement conditions were a spectral width of 69991.3 Hz, an acquisition time of 0.3 and 0.1 s relaxation delay between scans. The pulse width setting was 8.0 μs. The ^{119}Sn nucleus was externally referenced to $(CH_3)_4$Sn at room temperature. All NMR samples were prepared by dissolving 0.2 mmol of the sample in 2 mL of solvent (FM or H_2O) at about 60 °C.

Small Angle X-Ray Scattering (SAXS) Analysis. Small angle X-ray scattering (SAXS) was carried out with a Bruker Hi-star two-dimensional area detector (512 × 512 pixels) coupled with an Elliott GX3 microfocusing Cu rotating anode operated at 40 kV and 13 mA (0.01 < q <0.6 Å^{-1}). Measurements were performed by transmission in gently grounded samples and held in a custom built cell. The sample cell was a Kapton-windowed (∼4 mm width) cell in ∼40 μm thick zirconium metal foil (1 cm × 2 cm). The sample to detector distance and the center of the beam were precisely determined by calibration with Ag-behenate diffraction standard (d_{001} = 5.838 nm). The diffraction intensities of two-dimensional (2-D) collected images were integrated to yield one-dimensional (1D) diffraction patterns as a function of the wave vector q with the Fit2D program.[43] The wave vector q is defined as $q = 4\pi \sin \theta/\lambda$, where 2θ is the scattering angle. Scattering data were corrected for dark current and empty cell scattering.

Preliminary attempts to determine the Porod constant (K) in the pristine C_{18}PyPt_Ge_2Se_6 sample were unsuccessful with the Bruker Hi-star system. The appearance of the first (100) Bragg diffraction peak in the relatively low q region masked the Porod region. To determine well the Porod constant (K) in the pristine C_{18}PyPt_Ge_2Se_6 sample, measurements were performed with a Rigaku X-Max 3000 High Brilliance SAXS system equipped with Cu rotating anode operated at 40kV and 86mA and equipped with a multilayer mirror and 2D wire detector. The sample to detector distance was set to ∼150 cm to increase resolution of the scattering curve in the low q region (0.01 < q < 0.15 Å^{-1}).

Pair Distribution Function (PDF) Analysis. Diffraction experiments for pair distribution function analysis (PDF) were performed at the Advanced Photon Source (APS) located at Argonne National Laboratory, Argonne, Illinois using the high energy X-rays with the powder samples packed in 1 mm glass capillary. For data collection, an X-ray energy of 77.528 keV (λ = 0.15992 Å) was used to record diffraction patterns to high values of momentum transfer while eliminating fluorescence from the sample. The two-dimensional images were integrated within Fit2D to obtain the one-dimensional powder diffraction pattern, masking areas obscured by the beam stop arm.[43] The PDFs, $G(r) = 4\pi r[\rho(r) - \rho_o]$ where $\rho(r)$ and ρ_o are the instantaneous and average densities, were

(39) Mccarthy, T. J.; Ngeyi, S. P.; Liao, J. H.; Degroot, D. C.; Hogan, T.; Kannewurf, C. R.; Kanatzidis, M. G. *Chem. Mater.* **1993**, *5*, 331–340.
(40) Perrin, C. L.; Dwyer, T. J. *Chem. Rev.* **1990**, *90*, 935–967.
(41) Milne, J.; Williams, A. J. *Inorg. Chem.* **1992**, *31*, 4534–4538.
(42) Wynants, C.; Vanbinst, G.; Mugge, C.; Jurkschat, K.; Tzschach, A.; Pepermans, H.; Gielen, M.; Willem, R. *Organometallics* **1985**, *4*, 1906–1909.
(43) Hammersley, A. P.; Svensson, S. O.; Hanfland, M.; Fitch, A. N.; Hausermann, D. *High Press. Res.* **1996**, *14*, 235–248.
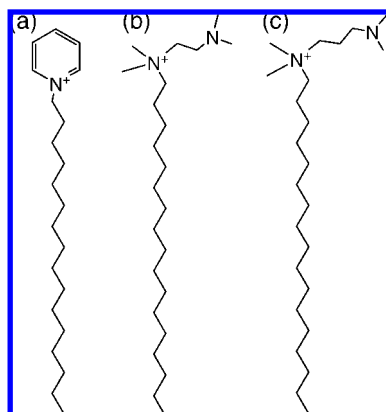
Figure 1. Surfactants used in this study: (a) C_nPyBr ($n = 14$ to 20), (b) $C_nTMEDABr$ ($n = 20, 22$), and (c) $C_nTMPDABr$ ($n = 20, 22$).

Figure 2. Low angle X-ray powder diffraction patterns of $C_nPyPt\_Ge_2Se_6$, where: (a) $n = 14$, (b) $n = 16$, (c) $n = 18$, and (d) $n = 20$ (lamellar).

extracted using PDFgetX2,[44,45] subtracting the contributions from the sample environment and background to the measured diffraction intensities. Corrections for multiple scattering, X-ray polarization, sample absorption, and Compton scattering were then applied to obtain the structure function $S(Q)$. Direct Fourier transform of the reduced structure function $F(Q) = Q[S(Q) - 1]$ yielded $G(r)$, the pair distribution function.

Density Measurements. The density of the materials was measured by a Micromeritics AccuPyc 1340 gas pycnometer (1 cm³ model) using ultra high purity (UHP) helium gas. About 200 mg sample was used for the measurements. Analysis run cycles were continued until a standard deviation of ± 0.0002 cm³ was obtained for the sample volume.

Results and Discussion

New mesostructured materials starting from $[Ge_2Se_6]^{4-}/Pt^{2+}$ and $[GeSe_4]^{4-}/Pt^{2+}$ combinations were prepared having hexagonal pore order, good thermal stability, reversible ion-exchange properties and strong absorption in the visible spectrum. Previous work with the monomeric $[SnQ_4]^{4-}$ (Q = Se, Te) clusters indicated the presence of solution equilibria and multiple building units, some or all of which could be incorporating in the final structure thereby playing a role in influencing the pore order.[28] Many questions however still remain unanswered. The temperature dependence of equilibrium is one of the most important issues to be understood since all templated assembly reactions are performed within a certain temperature range (between 60 and 100 °C). To study the precursor anions in solution and gain additional insights regarding speciation in water and FM solutions, we used ^{77}Se NMR and FAB MS.

Long Range Periodicity: Role of Surfactant and Inorganic Cluster. In this work, we employed surfactants with three different head-groups and variable chain lengths to observe their effect on long-range pore periodicity and other properties of the templated materials. In addition to the most commonly used pyridinium surfactant,[28] we also employed surfactants with tetramethyl-propanediamine (TMPDA) and tetramethyl-ethanediamine (TMEDA) as the head groups, Figure 1. The effective headgroup areas[46] of these two surfactants are significantly larger than that of the pyridinium-based ones. The $C_nPyBr/$
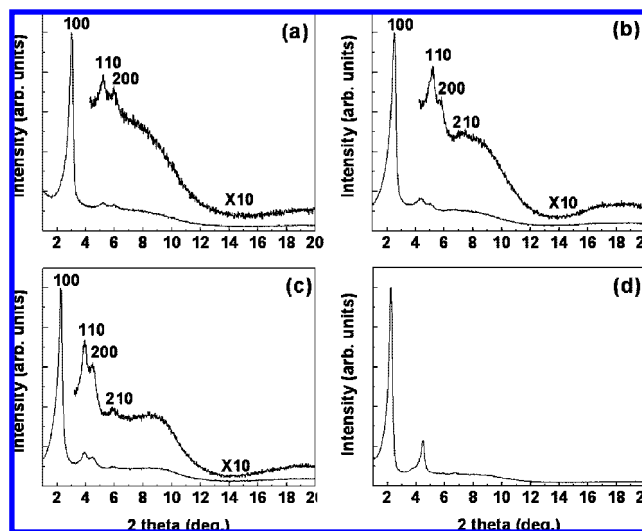
$K_4Ge_2Se_6/Pt^{2+}$ system gave hexagonal pore symmetry from $n = 14$ to $n = 18$ and lamellar structure at $n = 20$. In the case of $C_nTMPDABr$ and $C_nTMEDABr$ surfactants, hexagonal materials were formed even at $n = 22$. This can be rationalized in terms of surface curvature of the cylindrical micelle formed.[46] The larger head groups of $C_nTMPDABr$ and $C_nTMEDABr$ create cylindrical micelles with larger surface and greater curvature[46] and can thus accommodate the inorganic clusters around it without forming lamellar phases up to $n = 22$. The decrease in cylindrical surface area for C_nPyBr allows the $[Ge_xSe_y]^{z-}$ anions to pack more tightly resulting in lamellar phases for $n > 18$.

In X-ray diffraction, all samples (except $n = 20$) showed three or four well-defined Bragg reflections in the $2° < 2\theta < 7°$ region as shown in Figure 2, characteristic of a regular hexagonal pore arrangement similar to those of mesostructured silica MCM-41. In the $K_4Ge_2Se_6/Pt^{2+}/C_nPyBr$ system, the highest hexagonal pore order was found when $n = 18$, as evidenced by the more intense and sharper higher order reflections (110) and (200), as well as the observation of the fourth (210) reflection, Figure 2c. The materials do not show Bragg reflections above 10 deg in 2θ indicating the inorganic frameworks are nonperiodic.

The extended hexagonal pore structure is revealed by TEM, Figure 3. The wall thickness of the $C_{18}PyPt\_Ge_2Se_6$ compound is ~ 2.2 (± 0.1) nm and pore diameter $\sim 2.4(1)$ nm. Pore-pore spacing of 4.3(2) nm obtained from the TEM image is in good agreement with the X-ray diffraction data. In the case of $[Ge_4Se_{10}]^{4-}/Pt^{2+}/C_nPyBr$ combination described previously,[24] however, hexagonal pore symmetry was observed even when $n = 22$ due to the larger cluster size of $[Ge_4Se_{10}]^{4-}$ compared to $[Ge_2Se_6]^{4-}$.[24]

The $C_nTMPDABr$ family of surfactants also gave hexagonal structures with the highest degree of order observed for $n = 20$. This is indicated by the four sharp well resolved Bragg peaks in the X-ray diffraction pattern of Figure 4, and also the clear TEM image shown in Figure 5. The pore-pore distance, here increased slightly to 4.54 nm compared to the pyridinium analogue. For the $C_nTMEDABr$ class of surfactants, the sharpest powder X-ray diffraction pattern was obtained when $n = 22$, but still in this case the (110) and (200) peaks were not as well resolved as with the other family of surfactants, Figure 6.

(44) Egami, T.; Billinge, S. J. L. *Underneath the Bragg Peaks: Structural Analysis of Complex Materials*; Pergamon Press: Amsterdam, 2003.
(45) Qiu, X.; Thompson, J. W.; Billinge, S. J. L. *J. Appl. Crystallogr.* **2004**, *37*, 678.
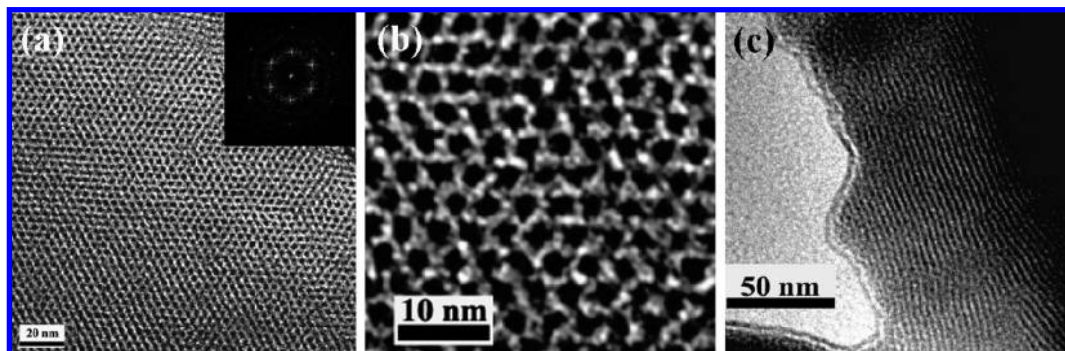(46) Huo, Q. S.; Margolese, D. I.; Stucky, G. D. *Chem. Mater.* **1996**, *8*, 1147–1160.

Figure 3. TEM images (a and b) of $C_{18}PyPt\_Ge_2Se_6$ prepared in FM down the pore channel axis and (c) perpendicular to pore channel axis. Inset of (a) shows corresponding Fourier transform.
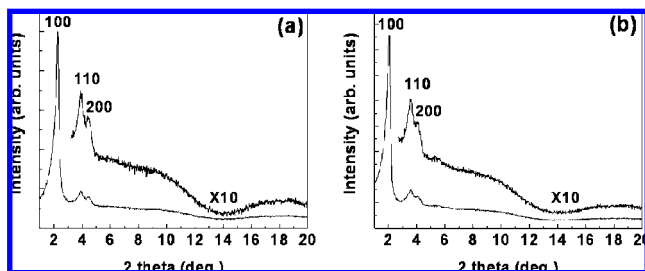

Figure 4. Low angle X-ray powder diffraction patterns of $C_nTMPDAPt\_Ge_2Se_6$, where: (a) $n = 20$ and (b) $n = 22$.

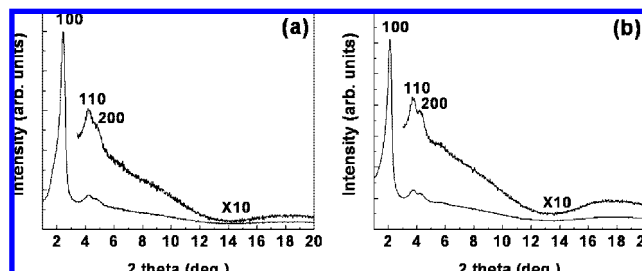**Figure 6.** X-ray powder diffraction patterns of $C_nTMEDAPt\_Ge_2Se_6$ (a) $n = 20$ and (b) $n = 22$.

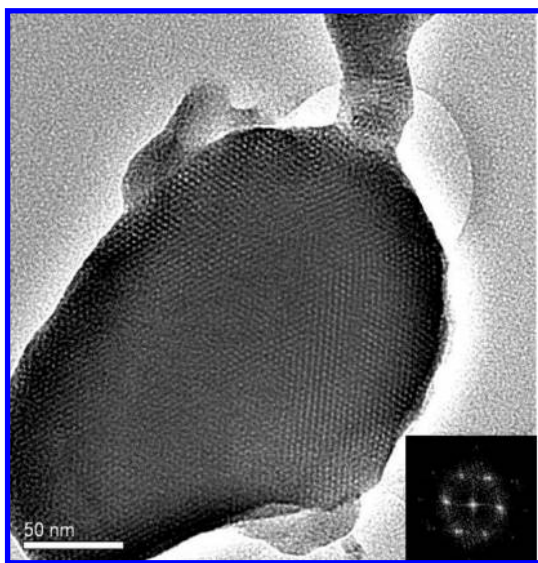**Figure 5.** Typical TEM image of $C_{22}TMPDAPt\_Ge_2Se_6$ along the (100) direction and the corresponding Fourier transform; larger particle showing hexagonal arrangement extending over its entire body.

Nevertheless, clear hexagonal pore organization was observed from TEM images in Figure 7.

Reactions with the $[Ge_2Se_6]^{4-}/Pt^{2+}/C_{16}PyBr$ combination in water also led to similar ordered hexagonal pore symmetry as evidenced by four sharp low angle Bragg peaks and the definitive hexagonal TEM image in Figure 8. The unit cell constant of this material was found to be 0.9 Å longer than that of the corresponding material made in FM under similar conditions.

In the $K_4GeSe_4/Pt^{2+}/C_nPyBr$ system good hexagonal order was observed when $n = 14$. Four well resolved, intense, sharp peaks in the range of $2° < 2\theta < 8°$ were obtained in the powder

XRD as shown in Figure 9. Moving to higher surfactant chain length did not improve the degree of pore organization, while a lamellar phase was obtained for $n = 20$. This underscores the necessity of higher surface curvature to obtain good long-range periodicity for this smaller cluster.

Table 1 shows trends of hexagonal unit cell constants with surfactant chain length and starting building blocks. The cell a constant gradually increases from 33.7(1) to 44.6(1) Å along the $C_nPyPt\_Ge_2Se_6$ series ranging from C_{14} to C_{18} hydrocarbon chain length.

Optical Properties. The optical absorption properties of the title materials show clear energy gaps are in the range of 1.24−1.97 eV, see Figure 10 and Table 2. There is a significant variation in the energy gap considering the inorganic framework is always "Pt/Ge/Se". As we will argue below, the exact Pt/Ge/Se composition changes with surfactant and with carbon tail length (n). In the $C_nPyPt\_Ge_2Se_6$ system, starting from $n = 14$ to $n = 20$ the energy gap gradually increases from 1.24 to 1.54 eV. This suggests that the inorganic walls change in thickness and or composition and it is consistent with the elemental analysis results shown in Table 2. For hexagonal pore packing, the inorganic wall is made up with two different structural regions: (a) wall lying between two adjacent pores (2-WR) and (b) wall lying between three such pores (3-WR).[28] The amount of Pt/Ge/Se material found in the 2-WR and 3-WR regions gradually changes with surfactant length and this creates changes in band gap energy. In other words changing the value of n does not produce rigorous analogs as the formulas $C_nPyPt\_Ge_2Se_6$ would imply but homologues with varying composition. A similar trend was previously observed in the $c\text{-}C_nPyPtSnSe$ ($n = 18$ and 20) system,[26] where moving to higher surfactant chain length band gap also increased. Figure 10b further shows increase in band gap energies of $C_{22}TMPDAPt\_Ge_2Se_6/C_{22}TMEDAPt\_Ge_2Se_6$ compared to those of $C_{20}TMPDAPt\_Ge_2Se_6/ C_{20}TMEDAPt\_Ge_2Se_6$.

In addition to changing the surfactant chain length, the effective tuning of the band gap can also be achieved by
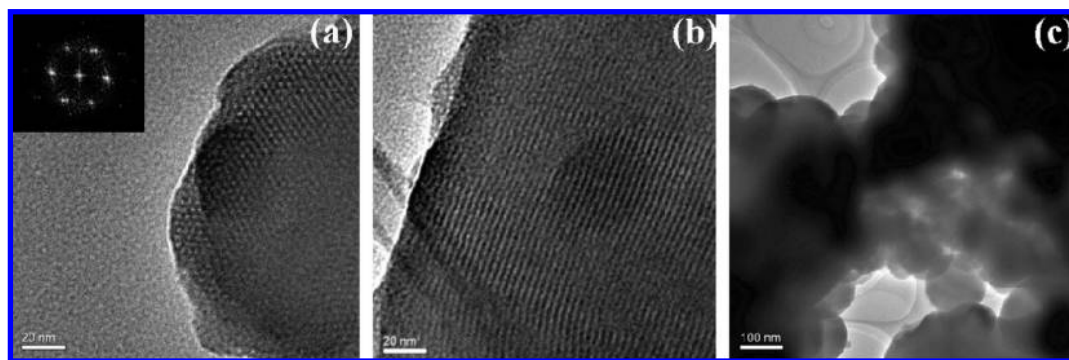
Figure 7. TEM images of $C_{22}TMEDAPt\_Ge_2Se_6$ (a) down the pore tunnel axis and corresponding Fourier transform (inset), (b) perpendicular to the pore tunnels, and (c) showing spherical particles of ∼100 nm size.
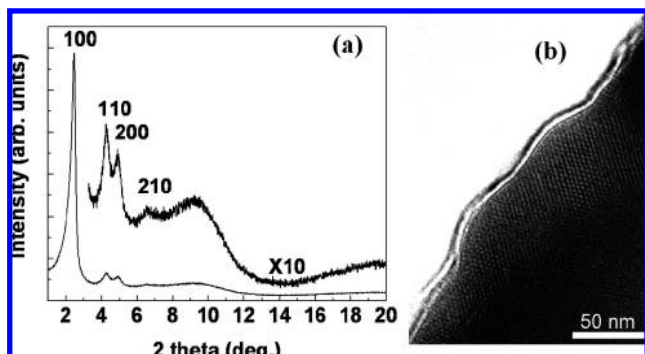

Figure 8. (a) Low angle X-ray powder diffraction patterns of $C_{16}PyPt\_Ge_2Se_6$ prepared in water and (b) its representative TEM image.
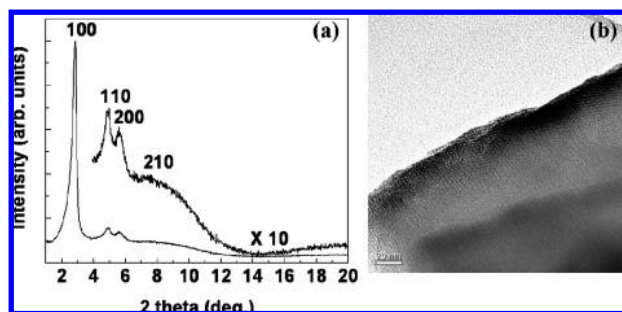

Figure 9. (a) Low angle X-ray powder diffraction patterns of $C_{14}PyPt\_GeSe_4$ and (b) its representative TEM image.

Table 1. Observed Bragg Reflections and Indexing for Mesostructured Platinum Germanium Selenides

mesophase	d_{100}, Å	d_{110}, Å	d_{200}, Å	d_{210}, Å	hexagonal unit cell constant, Å[a]
$C_{14}PyPt\_Ge_2Se_6$	29.1	16.8	14.6		33.7
$C_{16}PyPt\_Ge_2Se_6$	35.0	20.2	17.5	13.2	40.4
$C_{16}PyPt\_Ge_2Se_6$[b]	35.7	20.7	17.8	13.5	41.3
$C_{18}PyPt\_Ge_2Se_6$	38.7	22.3	19.4	14.6	44.6
$C_{20}PyPt\_Ge_2Se_6$	39.4		19.6		lamellar
$C_{20}TMPDAPt\_Ge_2Se_6$	39.1	22.9	19.7		45.4
$C_{22}TMPDAPt\_Ge_2Se_6$	42.9	24.6	21.5		49.5
$C_{20}TMEDAPt\_Ge_2Se_6$	36.2	21.1	18.4		42.1
$C_{22}TMEDAPt\_Ge_2Se_6$	41.6	23.8	20.7		47.8
$C_{14}PyPt\_GeSe_4$	30.9	17.8	15.4	11.6	35.6

[a] Estimated standard deviation ± 0.1 Å. [b] Sample prepared in water. All others prepared in FM.
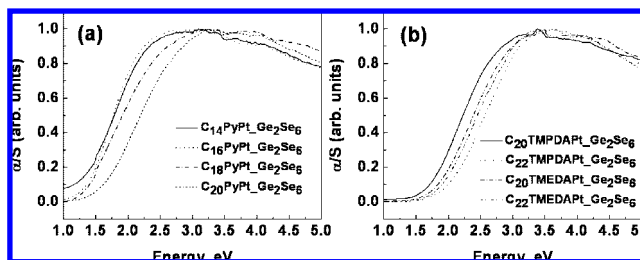

Figure 10. Solid-state UV−vis absorption spectra of (a) $C_nPyPt\_Ge_2Se_6$ and (b) $C_nTMPDAPt\_Ge_2Se_6$ and $C_nTMEDAPt\_Ge_2Se_6$ materials (all prepared in FM).

changing the building unit in the precursor solution. Starting with $[GeSe_4]^{4-}$ unit, material with lower band gap and well ordered structure was observed in $C_{14}PyPt\_GeSe_4$. Differences in band gap energies (1.31 vs 1.78 eV) for $C_{16}PyPt\_Ge_2Se_6$ prepared in FM and water were also observed and they might also arise from higher fraction of $[Ge_4Se_{10}]^{4-}$ incorporation in water (consistent with the NMR spectra discussed in the following section). The band gap energies obtained in this study lie in the same range as several important semiconductors (e.g., InP, GaAs, CdSe, CdTe etc.) suggesting possible interest in optoelectronic investigations.

Solution Behavior of $[Ge_2Se_6]^{4-}$. A study of the solution behavior of the precursor chalcogenido ions can answer several important questions: does the precursor building block remain intact in solution? What happens with the species during mesophase synthesis at 75 °C? What is the fate of the dissolved species with the addition of a Lewis acid (i.e., linking metal)?

Answers to these issues may help in understanding the composition and origin of pore order in these materials.

Although, some multinuclear NMR spectroscopy studies have been reported with $[SnSe_4]^{4-}$, $[SnTe_4]^{4-}$, $[Sn_2S_6]^{4-}$, $[SnS_4]^{4-}$, similar studies with the germanium analogs are few.[25,28,47] Earlier literature on the Ge/S system in water by Krebs et al. pointed out the presence of multiple species.[48] To our best knowledge the present work includes the first solution studies ever reported on the $[Ge_xSe_y]^{z-}$ system.

The ^{77}Se NMR spectrum of $K_4Ge_2Se_6$ in FM at 25 °C contained several signals among which those at ∼620 and ∼265 ppm are assigned to respective bridging and terminal selenium atoms of the $[Ge_2Se_6]^{4-}$ anion, see Figure 11a.[49] The remaining peaks however belong to different species. The tiny peaks at

(47) Melullis, M.; Dehnen, S. *Z. Anorg. Allg. Chem.* **2007**, *633*, 2159–2167.
(48) Krebs, B. *Angew. Chem., Int. Ed. Engl.* **1983**, *22*, 113–134.
(49) The peak positions are temperature and concentration dependent. Varying the temperature and or concentration causes spectral shift.

Table 2. Elemental Analysis, Colors, and Energy Band Gaps for Mesostructured Platinum Germanium Selenides

mesosphere	% C, H, N	Pt/Ge/Se Ratio[a]	energy gap[b] (eV)
$C_{14}PyPt\_Ge_2Se_6$	24.40:3.52:1.54	1.4:2:6.1	1.24
$C_{16}PyPt\_Ge_2Se_6$	30.51:4.81:1.82	1.4:2:6.2	1.31
$C_{16}PyPt\_Ge_2Se_6^c$	29.26:4.62:1.76	1.3:2:6.3	1.78
$C_{18}PyPt\_Ge_2Se_6$	36.31:5.75:1.89	1.3:2:6.2	1.41
$C_{20}PyPt\_Ge_2Se_6$	34.67:5.37:1.70	1.4:2:6.1	1.54
$C_{20}TMPDAPt\_Ge_2Se_6$	29.34:5.48:2.46	1.7:2:6.2	1.63
$C_{22}TMPDAPt\_Ge_2Se_6$	31.03:5.76:2.78	1.6:2:6.1	1.97
$C_{20}TMEDAPt\_Ge_2Se_6$	24.57:4.44:2.29	1.5:2:6.1	1.79
$C_{22}TMEDAPt\_Ge_2Se_6$	31.89:5.82:2.65	1.6:2:6.2	1.85
$C_{14}PyPt\_GeSe_4$	28.38:4.44:1.82	1.4:1:3.9	1.27

[a] Based on EDS results. Listed values are an average of five measurements on different areas of powder samples. [b] Determined by optical spectroscopy. [c] Sample prepared in water. All others prepared in FM. Color of all samples: dark brown red.

~157 and ~212 ppm are fingerprints of the respective terminal and bridging selenium atoms of the adamantane $[Ge_4Se_{10}]^{4-}$ anion in FM.[50] In addition, several weaker peaks at ~129, ~307, and ~340 ppm are consequently ascribed to respective terminal, Se_t, bridging μ_2-Se_{mb}, and bridging diselenide Se_{db} atoms of the $[Ge_2Se_7]^{4-}$ anion which is present as a minor impurity. The very weak resonance at ~27 ppm is that of the tetrahedral $[GeSe_4]^{4-}$ anion. The coexistence of $[Ge_2Se_6]^{4-}$ and $[Ge_4Se_{10}]^{4-}$ implies that they are in equilibrium (eq 1)

$$2[Ge_2Se_6]^{4-} \rightleftharpoons [Ge_4Se_{10}]^{4-} + 2Se^{2-} \qquad (1)$$
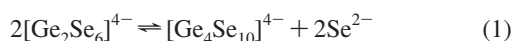
The $[Ge_2Se_7]^{4-}$ species likely was formed in solution by the reaction of Se^0 (traces of which could come from the starting materials) with the $[Ge_2Se_6]^{4-}$ anion (eq 2) or by the presence of some $K_4Ge_2Se_7$ in the starting material. This is consistent with earlier observations that $[Ge_2S_6]^{4-}$ is always found in equilibrium with $[Ge_2S_7]^{4-}$ and $[Ge_4S_{10}]^{4-}$.[48]

$$[Ge_2Se_6]^{4-} + Se^0 \rightleftharpoons [Ge_2Se_7]^{4-} \qquad (2)$$

The ^{77}Se NMR spectrum of $K_4Ge_2Se_6$ at 25 °C in aqueous solution shows a higher proportion of $[Ge_4Se_{10}]^{4-}$ compared to that in FM with no evidence of $[GeSe_4]^{4-}$, Figure 11b. This is consistent with the greater Bronsted acidity of water which favors the conversion of the more basic $[GeSe_4]^{4-}$ species to $[Ge_2Se_6]^{4-}$. This hypothesis is supported by the observed change in relative ratio of $[GeSe_4]^{4-}$ to $[Ge_4Se_{10}]^{4-}$ in FM after the addition of Ba^{2+} ions as a weak Lewis acid. Upon addition of $Ba(NO_3)_2$, the resulting NMR spectrum showed the disappearance of $[GeSe_4]^{4-}$, and the appearance of a significant higher fraction of $[Ge_4Se_{10}]^{4-}$. Conversely, the equilibrium can be reversed with the addition of base in the solution. Indeed, by increasing the pH to ~ 10−12 through the addition of KOH we observed no peaks of $[Ge_4Se_{10}]^{4-}$ in the NMR spectrum. At the same time the concentration of $[GeSe_4]^{4-}$ increased rapidly as shown in Figure 11c. In FM solution, the equilibrium could also be shifted quantitatively to the $[GeSe_4]^{4-}$ anion by adding K_2Se. The impurity $[Ge_2Se_7]^{4-}$, can be converted to $[Ge_2Se_6]^{4-}$ by adding PPh_3 which is a well-known chalcogen scavenger. The phosphine abstracts Se^0 from the Se_2^{2-} group forming Ph_3PSe, Figure 11d.

To confirm the above equilibria, we investigated the system further using two-dimensional NMR techniques. Magnetization transfer experiments can distinguish between species exchanging

in solution.[40] 2D EXSY is a powerful experiment capable of observing exchange between species.[41,42] At 60 °C, when we saturated the peaks of the anion $[Ge_2Se_6]^{4-}$, we observed saturation of the peaks of $[Ge_2Se_7]^{4-}$, confirming rapid exchange between the two. However, we did not observe any saturation of the peaks of $[Ge_4Se_{10}]^{4-}$ at this temperature. It is possible that the exchange is too fast to be observed in this time scale. In 2D EXSY experiments at 60 °C; however, we clearly observed off-diagonal cross peaks between $[Ge_2Se_6]^{4-}$ and $[Ge_2Se_7]^{4-}$ and also between $[Ge_2Se_6]^{4-}$ and $[Ge_4Se_{10}]^{4-}$, see Figure 12. We did not observe off-diagonal cross-peaks between $[Ge_2Se_7]^{4-}$ and $[Ge_4Se_{10}]^{4-}$ indicating no equilibrium between these species.

Variable temperature experiments showed that at 60 °C in FM the major species are $[Ge_2Se_6]^{4-}$ and $[Ge_4Se_{10}]^{4-}$ in almost equal proportion; whereas at 100 °C, the system gains $[Ge_4Se_{10}]^{4-}$ at the expense of $[Ge_2Se_6]^{4-}$. Cooling the solution to 25 °C, caused the characteristic peaks of the species present initially (i.e., $[Ge_2Se_6]^{4-}$, $[Ge_2Se_7]^{4-}$, $[Ge_4Se_{10}]^{4-}$, and $[GeSe_4]^{4-}$) to reappear, indicating complete reversibility and thus equilibria. Similar effects were observed in water as well. The spectroscopic observations described above are consistent with the solution equilibria shown in Scheme 1.

The spectroscopic results provide certain insights regarding mesostructured materials made in FM starting from $[Ge_2Se_6]^{4-}$ precursor. The presence of multiple species in solution during the preparation of mesophases and their rapid interconversion with temperature and presence of Lewis acid centers suggest it is unlikely that only a single species is incorporated in a given mesostructure. More probably, multiple species are incorporated simultaneously in the framework structure. Each of those species likely plays a vital role in building and stabilizing the overall mesostructure. A control experiment in which a mixture of selenogermante anions $[GeSe_4]^{4-}$ and $[Ge_4Se_{10}]^{4-}$ was used in a synthesis reaction (see Experimental Section) showed that the product obtained with both $C_{16}Py$ and $C_{18}Py$ surfactants possessed a hexagonal pore order identical to that observed in the materials described here prepared from single selenogermante anions.

Comparison of ^{119}Sn NMR spectrum of $[Sn_2Se_6]^{4-}$, $[SnSe_4]^{4-}$, and $[SnTe_4]^{4-}$ in FM with the presence of K_2PtCl_4 at least indicates that the cubic mesostructure is possible only when $[M_2Q_6]^{4-}$ is the single building unit present in FM (Supporting Information).[28] Even though $[SnSe_4]^{4-}$ almost completely converts to $[Sn_2Se_6]^{4-}$ in FM, traces of $[SnSe_4]^{4-}$ and additional unassigned species prevent the system from yielding cubic structures; hexagonal mesophases were formed instead. $[SnTe_4]^{4-}$ also behaved similarly and again no cubic structures were observed. The fact that $[Ge_2Se_6]^{4-}/Pt^{2+}$ combination does not afford any cubic structure analogous to the $[Sn_2Se_6]^{4-}/Pt^{2+}$ system is attributed to the participation of the $[Ge_2Se_6]^{4-}$ unit in equilibria producing additional species inappropriate for the cubic motif. For the hexagonal structures, however, the equilibria of $[Ge_2Se_6]^{4-}$ appears to be an advantage helping to achieve good pore order.[51]

FAB Mass Spectroscopic Support. FAB mass-spectroscopy of FM solutions of the precursor $K_4Ge_2Se_6$ in positive ionization mode showed peaks at *m/z* 776 and 814.5 due to $[Ge_2Se_6]^{4-}$ anion, Figure 13. On the basis of isotopic distribution patterns,

(50) ^{77}Se NMR spectra of $(TMA)_4Ge_4Se_{10}$ in FM consists of two distinct peaks at 156.6 and 212.7 ppm.

(51) Attempts to prepare mesophases after controlled suppression of $[Ge_4Se_{10}]^{4-}$ from solution with the addition of base (KOH) resulted disordered pore arrangement.
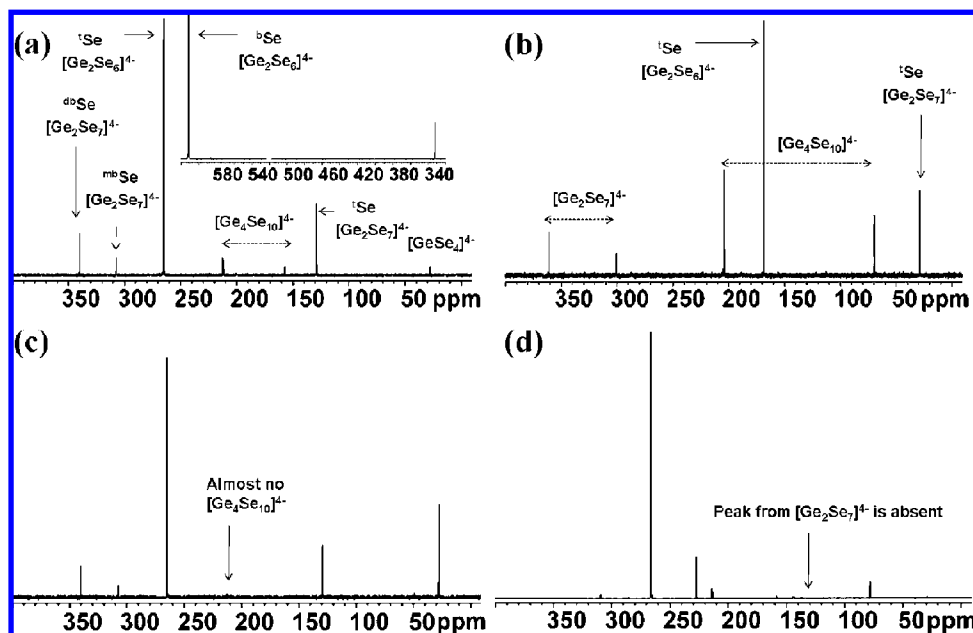
Figure 11. ^{77}Se NMR spectra of $K_4Ge_2Se_6$ dissolved in (a) FM, (b) H_2O, (c) FM and KOH, and (d) FM and PPh$_3$ (all spectra were taken at 25 °C).
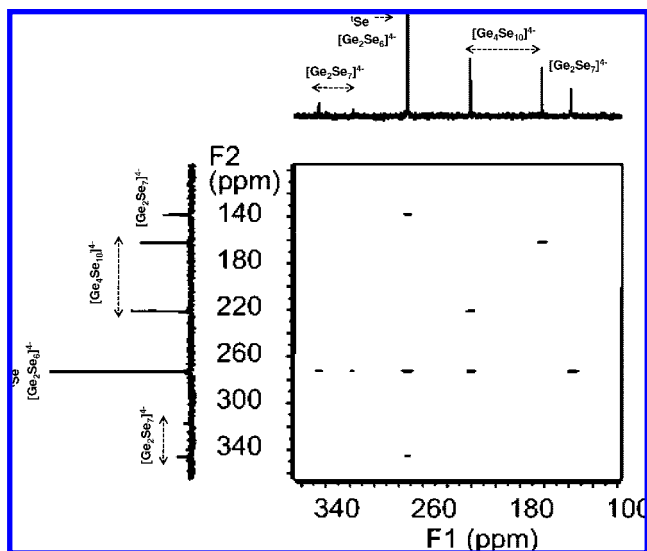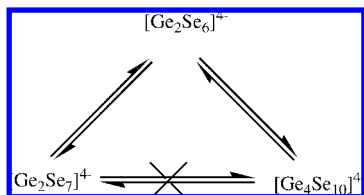

Figure 12. 2D-EXSY ^{77}Se NMR spectra (at 65 °C) of $K_4Ge_2Se_6$ dissolved in FM.

Scheme 1. Solution Equilibrium of $[Ge_2Se_6]^{4-}$ in FM

these peaks could be assigned to $[H(K_4Ge_2Se_6)]^+$ and $[K(K_4Ge_2Se_6)]^+$, respectively. Other peaks at m/z 855.5, 894, and 1275.5 could be matched with the isotopic distribution patterns of $[H(K_4Ge_2Se_7)]^+$, $[K(K_4Ge_2Se_7)]^+$, and $[K(K_4Ge_4Se_{10})]^+$, respectively. This supports the presence of those multiple species in FM solution.

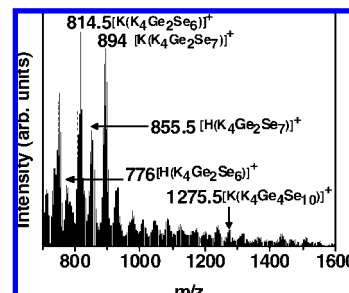**Raman and Far-IR Spectroscopy of *Surf*_Pt_Ge$_2$Se$_6$.** To probe the fate of $[Ge_2Se_6]^{4-}$ in the final mesostructured

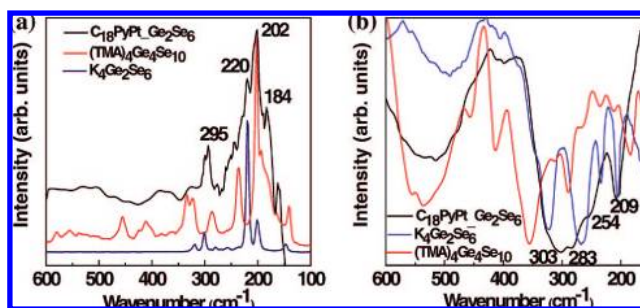**Figure 13.** FAB mass spectra of the precursor $K_4Ge_2Se_6$ in FM. Data was taken in the positive ionization mode.

Figure 14. Comparison of (a) Raman and (b) Far IR spectra of mesostructured compound with $[Ge_2Se_6]^{4-}$ and $[Ge_4Se_{10}]^{4-}$ clusters.

materials, we compared the Raman spectra with those of $K_4Ge_2Se_6$ and $(TMA)_4Ge_4Se_{10}$, Figure 14a. For $C_{18}PyPt\_Ge_2Se_6$, at least four peaks were observed in the $100-600$ cm^{-1} region. The sharp peak at 202 cm^{-1} is due to the combination of totally symmetric v_2 (A$_1$) breathing mode of the Ge$_4$Se$_6$ cage from the $[Ge_4Se_{10}]^{4-}$ unit and terminal v_{15} (B$_3$) Se—Ge—Se bending mode (might be overlapped with the v_6 (B$_1$) asymmetric Ge—Se stretching mode) from the $[Ge_2Se_6]^{4-}$ unit.[52–54] The peak at 220

(52) Krebs, V. B.; Muller, H. *Z. Anorg. Allg. Chem.* **1983**, *496*, 47–57.
(53) Campbell, J.; Devereux, L. A.; Gerken, M.; Mercier, H. P. A.; Pirani, A. M.; Schrobilgen, G. J. *Inorg. Chem.* **1996**, *35*, 2945–2962.
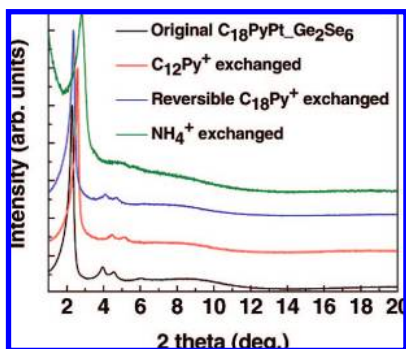
Figure 15. Low angle XRD of ion-exchanged materials. Reversible ion-exchange property of mesostructured $C_{18}PyPt\_Ge_2Se_6$ is demonstrated by the shift of Bragg diffraction peaks.
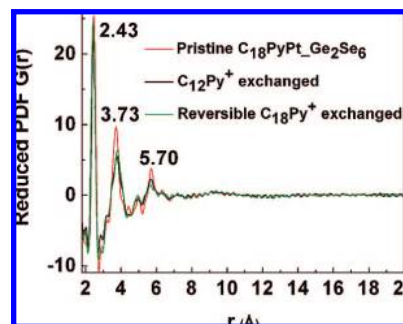

Figure 16. Reduced atomic pair distribution function G(r) of mesostructured $C_{18}PyPt\_Ge_2Se_6$ and its ion-exchanged materials as a function of interatomic distance r.

cm^{-1} resembles the symmetric v_2 (A_1) ring mode of the Ge_2Se_2 core in $[Ge_2Se_6]^{4-}$. The less intense peak centered around 295 cm^{-1} could be from the symmetric v_1 (A_1) and asymmetric v_{11} (B_2) terminal Ge−Se stretching modes. These were originally at 301 and 320 cm^{-1} respectively in $K_4Ge_2Se_6$; however, they shift slightly to lower frequency due to binding with the linking Pt^{2+} ion.

Comparison of vibrational frequencies of $C_{18}PyPt\_Ge_2Se_6$ with those of the $K_4Ge_2Se_6$ precursor and $(TMA)_4Ge_4Se_{10}$ in the far-infrared (IR) region clearly indicates the mesostructured material contains both $[Ge_2Se_6]^{4-}$ and $[Ge_4Se_{10}]^{4-}$ units, Figure 14b. Because of the presence of different bonding environments in the nonperiodic inorganic framework, the spectra are much broader compared to the free clusters, however, characteristic peaks from both $[Ge_2Se_6]^{4-}$ and $[Ge_4Se_{10}]^{4-}$ are evident. The slight shifts of the frequencies to lower energy are attributed to binding with the metal ions. The sharp peak at 209 cm^{-1} likely arises from the totally symmetric v_2 (A_1) ring mode from a Ge_2Se_2 fragment since it highly resembles that in $[Ge_2Se_6]^{4-}$.[52–54] It could be also possible that this comes from the spectral shift of the v_6 (B_1) vibration of $[Ge_2Se_6]^{4-}$. The v_{11} (T_2) and v_{12}(T_2) vibrational modes at 354 and 290 cm^{-1} wave numbers of $[Ge_4Se_{10}]^{4-}$ unit are shifted to 324 and 283 cm^{-1} respectively. Similarly, peaks from $[Ge_2Se_6]^{4-}$ at 322 and 267 cm^{-1} due to respective v_{11} (B_2) and v_1 (A_1) vibrations give respective signals at 303 and 254 cm^{-1} in the mesostructured material. Because the mesophase lacks long-range symmetry, clustering of these vibration modes causes a broad spectral hump.

Ion-Exchange Properties and Porosity. The pore accessibility of the chalcogenide materials was investigated by studying their ion-exchange properties with other cationic species. The powder diffraction data showed that the main Bragg diffraction peak of $C_{18}PyPt\_Ge_2Se_6$ is clearly shifted from 38.7 to 34.2 Å after exchange with $C_{12}PyBr$, Figure 15. The corresponding hexagonal unit cell parameter was reduced from 44.6(1) to 39.6(1) Å. Pyrolysis mass spectroscopy of the $C_{12}Py^+$ exchanged material showed a large peak at $m/z = 248.3$ ($C_{12}H_{25}Se$) and only a tiny one at $m/z = 332$, confirming the presence of mainly $C_{12}Py^+$ in the pores. Interestingly, the ion-exchanged material can expand its unit cell again after reverse exchange with $C_{18}Py^+$. The reverse exchanged material caused the main Bragg diffraction peak to shift from 34.2(1) Å to 37.4(1) Å corresponding to a unit cell expansion to 43.3(1) Å. The long-range pore order was maintained in $C_nPyPt\_Ge_2Se_6$ after reverse ion-exchange

as evidenced by the three sharp Bragg peaks. This reversible cell contraction and expansion, known as "breathing" behavior, is a rare property in framework materials and has been previously observed in mesostructured $c\text{-}C_nPyPtSnSe$ and $c\text{-}/h\text{-}C_nPyInSbSe$ systems.[27,30] The "breathing" behavior of these mesostructured materials is remarkable and appears to be a general property of chalcogenide mesostructured materials. Silica and other oxide mesostructured materials are rigid in this regard.

Attempts to exchange the surfactant inside the pore with very small cationic species such as NH_4^+ resulted in even larger unit cell contraction to 36.3(1) Å and the long-range pore ordering deteriorated. Elemental analysis indicated that almost all surfactant molecules were replaced with NH_4^+. Again $(NH_4)Pt\_Ge_2Se_6$ did not show open porosity because of the contraction of the flexible chalcogenide framework.

Pair Distribution Function (PDF) Analysis. To probe the local structures of the nonperiodic mesostructured framework, we used the PDF technique which analyses both diffuse and Bragg scattering.[55] This allows to determine the interatomic distances between various neighbors in the structure and thus gain local structure information about the building units present in the structure. Figure 16 shows PDF plots as a function of interatomic distance for pristine and ion-exchanged $C_{18}PyPt\_Ge_2Se_6$ material. The PDF of pristine $C_{18}PyPt\_Ge_2Se_6$ material showed up to three sharp correlation vectors. The first correlation vector at $\sim$2.43 Å arises from the first neighbor Ge−Se and Pt−Se bond distances. The peak at $\sim$3.73 Å could be from the second neighbor Ge−Ge or Se−Se or Pt−Ge distances. The lack of well defined features in the PDF beyond $\sim$6 Å suggests the local order is limited in a volume of material with $\sim$6 Å diameter. Beyond this distance the randomness of the inorganic network predominates. The material exchanged with $C_{12}Py^+$ and then reverse ion-exchanged with $C_{18}Py^+$ displays similar PDF correlations at the same distances as observed in the pristine $C_{18}PyPt\_Ge_2Se_6$ material indicating that the local inorganic framework remains intact during the ion-exchange process. This suggests that the observed flexibility of the Pt/Ge/Se network that allows it to expand and contract in response to ion-exchange is due to changes in bond angles and dihedral angles and not to changes in bonding.

Stability. Investigations of the thermal stability of $C_{16}PyPt\_Ge_2Se_6$, $C_{20}TMPDAPt\_Ge_2Se_6$, $C_{20}TMEDAPt\_Ge_2Se_6$ and $C_{14}PyPt\_GeSe_4$ were carried out with TGA and pyrolysis MS-experiments. The TGA curves in Figure 17 indicate that

(54) Campbell, J.; Diciommo, D. P.; Mercier, H. P. A.; Pirani, A. M.; Schroblgen, G. J.; Willuhn, M. *Inorg. Chem.* **1995**, *34*, 6265–6272.

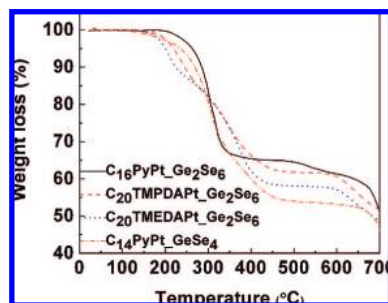(55) Billinge, S. J. L.; Kanatzidis, M. G. *Chem. Commun.* **2004**, *7*, 749–760.

Figure 17. Typical TGA curves of $C_{16}PyPt\_Ge_2Se_6$, $C_{20}TMPDAPt\_Ge_2Se_6$, $C_{20}TMEDAPt\_Ge_2Se_6$ and $C_{14}PyPt\_GeSe_4$ at 20 °C per minute heating rate under nitrogen flow.

all materials undergo a two-step (at least) weight loss between 160 and 470 °C and it is due to surfactant decomposition. Common trends were observed for each surfactant class. The pyridyl headgroup and $C_nH_{2n+1}Se^+$ are typical decomposition species for all C_nPy mesostructured chalcogenides.[28] The $C_nTMPDABr$ and $C_nTMEDABr$ templated compounds show different decomposition products during thermal treatment.

For $C_nTMPDAPt\_Ge_2Se_6$ between 160 and 470 °C, the major decomposition products evolved were $N(CH_3)_3$, $N(CH_3)_2$-$CH_2CH_2CH_3$, $N(CH_3)_2CH_2CH_3$ and $C_nH_{2n+1}N(CH_3)_2$. In the case of $C_nTMEDAPt\_Ge_2Se_6$, the inorganic framework also started decomposing in this temperature region eliminating fragments of R-Se$^+$ along with $N(CH_3)_3$, $N(CH_3)_2CH_2CH_3$ and $C_nH_{2n+1}N(CH_3)_2$. The difference in thermal behavior between the two surfactant types can be rationalized in terms of the different degree of interaction with the inorganic framework. Above 570 °C rapid collapse of the inorganic structures occurs with the fragments of $(CH_3)_2(CH_2CH_3)N-Se^+$ and $N(CH_3)_2^+$ being the main detectable species. At 750 °C, a mixture of amorphous and partly crystalline PtGeSe phase was detected.[56]

Small Angle X-ray Scattering. Because of the presence of surfactants in the pore of $C_nPyPt\_Ge_2Se_6$ direct gas absorptions measurements could not be made to determine the surface area. In such cases small-angle X-ray scattering (SAXS) is a powerful technique that can be used to obtain the underlying surface area of the inorganic framework. It is important to note that SAXS is sensitive to differences in electron density at the wall-pore interface and for this reason it can be used to determine the area of the surfactant/Pt−Ge−Se interface by analyzing the Porod region. The latter can give information about both closed and open porosity, thereby giving a good estimation of the potential free space and surface area in the system.[57−62]

The SAXS curve usually displays fractal behavior as expressed by the intensity ($I(q)$) vs scattering vector, q plot according to the equation, $I(q) = k.q^{-\alpha}$, where $q = 4\pi \sin \theta/\lambda$, θ is the scattering angle, λ is the wavelength, k is a constant, α

is related to the fractal dimension. It follows Porod's law at a large value of the q vector and a limiting behavior is observed: $\lim q \to \infty \, I(q) = K/q^3$ (K is the Porod constant).[58] The specific surface area (S_{SAXS}) is then determined using the method of the invariant (where b is the background intensity)

$$Q = \int_{q_{min}}^{q_{max}} (I(q) - b)q^2 dq + \frac{K}{q_{max}} \qquad (3)$$

$$S = \pi\varphi(1 - \varphi)\left(\frac{K}{\rho Q}\right) = \pi\varphi\left(\frac{K}{\rho_s Q}\right) \qquad (4)$$

where the Porod constant $K = \lim q \to \infty \, \{I(q)q^3\}$, φ is the volume fraction of framework voids, ρ, ρ_s are the bulk and skeletal mass density respectively (where $\rho/\rho_s = 1 - \varphi$), and Q is the invariant parameter defined as the q^2 weighted integrated intensity $I(q)$ of the scattering curve according to eq 3.

Because almost all surfactant molecules were replaced by NH_4^+ ions in $(NH_4)Pt\_Ge_2Se_6$, SAXS surface area (S_{SAXS}) analysis was performed on this sample and compared with that of the pristine $C_{18}PyPt\_Ge_2Se_6$. To determine the specific surface area of the pristine $C_{18}PyPt\_Ge_2Se_6$, $I(q)q^3$ vs q^3 was plotted in the Porod region (q of 0.032 to 0.066 Å^{-1}) and a K value of 0.09 was obtained from the intercept (Supporting Information).[58] The Q value was determined from eq 3 where the upper limit, q_{max} was evaluated by arbitrarily choosing a q value and fitting with $\int_{q_{min}}^{\infty} (I(q) - b)q^2 dq \approx K/q_{max}$.[61,62]

Figure 18a shows the intensity $I(q)$ falls gradually for pristine $C_{18}PyPt\_Ge_2Se_6$ until $q=0.08$Å^{-1} followed by the Bragg peak at q $\sim$ 0.15 Å^{-1}. Based on the measured skeletal density[63] of $\sim$5.1 g/cm^3 and bulk density of 1.67 g/cm^3 for the pristine $C_{18}PyPt\_Ge_2Se_6$, we obtained 331 m^2/g surface area (S_{SAXS}) for the inorganic framework. Similar measurement with the ion-exchanged material $(NH_4)Pt\_Ge_2Se_6$,[64] shows 250 m^2/g surface area (S_{SAXS}). These potential surface areas are very large and correspond to $\sim$1688 and $\sim$1275 m^2/g silica equivalent areas, respectively.[65]

From the $\ln[I(q)]$ vs $\ln[q]$ plot in Figure 18b in the Porod region, two distinct slopes of 2.38 and 1.27 were obtained, indicating two different mass fractal behaviors.[66] Thus though particles are connected in a three-dimensional like pattern, the low mass fractality (<3) reflects the hollow nature of the framework and thereby the enormous surface area of the inorganic framework available in $(NH_4)Pt\_Ge_2Se_6$. Pristine $C_{18}PyPt\_Ge_2Se_6$ showed a mass fractality of 2.90.

Average chord length (l_p)[59] of the pores of the ion-exchanged sample as determined by $l_p = l/\varphi_s$ (where $l = 4Q/\pi K$ and φ_s is the volume fraction of solid part) turns out to be $\sim$2.5 nm which is consistent with the pore diameter measured by TEM for the pristine $C_{18}PyPt\_Ge_2Se_6$. The average pore diameter can also

(56) Abrahams, S.; Bernstein, J. L. *Acta Cryst. B* **1977**, *33*, 301.
(57) Ne, F.; Zemb, T. *J. Appl. Crystallogr.* **2003**, *36*, 1013–1018.
(58) Li, Z. H.; Gong, Y. J.; Wu, D.; Sun, Y. H.; Wang, J.; Liu, Y.; Dong, B. Z. *Surf. Interface Anal.* **2001**, *31*, 897–900.
(59) Dieudonne, P.; Delord, P.; Phalippou, J. *J. Non-Cryst. Solids* **1998**, *225*, 220–225.
(60) Donatti, D. A.; Ruiz, A. I.; Vollet, D. R. *J. Non-Cryst. Solids* **2001**, *292*, 44–49.
(61) Ehrburger-Dolle, F.; Fairen-Jimenez, D.; Berthon-Fabry, S.; Achard, P.; Bley, F.; Carrasco-Marin, F.; Djurado, D.; Moreno-Castilla, C.; Morfin, I. *Carbon* **2005**, *43*, 3009–3012.
(62) Fairen-Jimenez, D.; Carrasco-Marin, F.; Djurado, D.; Francoise, B.; Ehrburger-Dolle, F.; Moreno-Castilla, C. *J. Phys. Chem. B* **2006**, *110*, 8681–8688.

(63) The skeletal density was measured using helium pycnometry. Here it is assumed that helium penetrates throughout the pores and accounts only the volume of the inorganic wall. However, since helium cannot penetrate through the surfactant occupied pores of pristine $C_{18}PyPt\_Ge_2Se_6$, the bulk density of this material was assumed to be its helium density.
(64) The bulk and skeletal densities of $(NH_4)Pt\_Ge_2Se_6$ are 2.16 and 5.10 g/cm^3 respectively.
(65) The empirical formulas of the inorganic framework were normalized to two selenium atoms to compare well with SiO$_2$ for equivalent surface area calculation.
(66) Vollet, D. R.; Donatti, D. A.; Ruiz, A. I. *J. Non-Cryst. Solids* **2001**, *288*, 81–87.
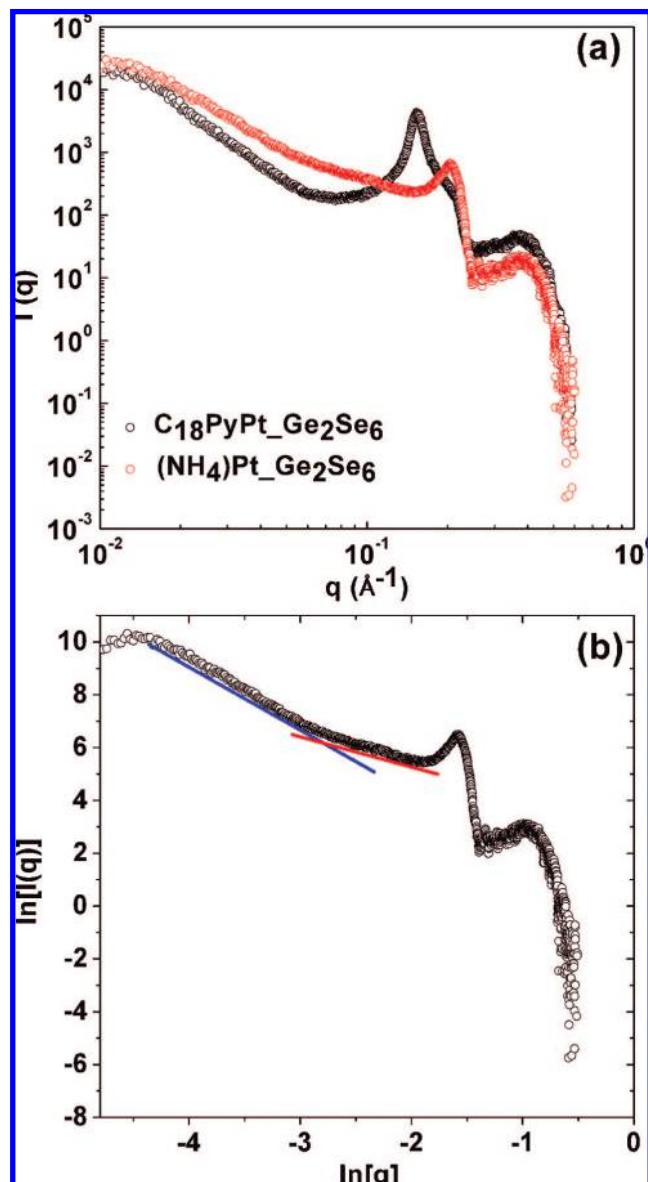
Figure 18. Small angle X-ray scattering (SAXS) data of pristine $C_{18}PyPt\_Ge_2Se_6$ and ion-exchanged material $(NH_4)Pt\_Ge_2Se_6$. (a) Intensity $I(q)$ versus q plot (data presented in the log scale). (b) Porod's plot of $\ln[q]$ vs $\ln[I(q)]$ for $(NH_4)Pt\_Ge_2Se_6$.

be calculated by plotting $I(q)^{-1/2}$ vs θ^2 (in radians)[67] and was found to be ~2.6 nm for $(NH_4)Pt\_Ge_2Se_6$ in good agreement with the TEM observations described above. The SAXS results clearly imply that despite the collapse of pore order, the inorganic framework in the ion exchanged material preserves

(67) Longman, G. W.; Wignall, G. D.; Hemming, M.; Dawkins, J. V. *Colloid Polym. Sci.* **1974**, *252*, 298–305.

the characteristic features of the pristine parent sample and retains its enormous surface area.

Concluding Remarks

In the synthesis of mesophases, starting with the anionic $[Ge_2Se_6]^{4-}$ chalcogenide cluster, a single species is not involved; rather multiple species are present and likely participate in the assembly. Even though temperature can favor one species over another, varying the temperature or adding the linking metal ion in the system alters the relative concentration of those species. Surfactant variation influences the composition of the mesophase materials thereby tuning their band gap transitions. This could be an attractive route to changing systematically the electronic functionality of these materials. Depending upon the specific conditions, the mesostructured materials can possess various anionic building blocks and the optoelectronic properties are dictated mainly by relative population of those building units. Thus, mesostructured chalcogenides with variable energy gap and pore symmetry are now available for further manipulation.

Our current and previous work on $Pt^{2+}/[SnSe_4]^{4-}$, $Pt^{2+}/[SnTe_4]^{4-}$, $Pt^{2+}/[Sn_2Se_6]^{4-}$, $Pt^{2+}/[Sn_4Se_{10}]^{4-}$ systems suggests that the adoption of a particular symmetry, for example, wormhole vs cubic vs hexagonal, in mesostructured chalcogenides is largely inherent in the selection of building units. The fact that surfactant size, shape, concentration, solvent, coordination preference of the linking metal ion and kinetics of the metathesis reaction also contribute to the final pore symmetry underscore the great complexity of these directed self-assembly reactions.

Even though surfactant-containing crystalline mesoporous chalcogenides have not been reported to date, the more appreciated role of solution equilibria during directed assembly of these structures could provide useful insights on selecting building units and solvents for controlling pore order and ultimately crystallinity. The demonstrated reversible ion-exchange property of these systems illustrates that optically and electronically active guest species could be incorporated into the pores to create novel organic–inorganic junctions.

Supporting Information Available: ^{119}Sn NMR spectra of neat $(TMA)_4Sn_4Se_{10}$, neat $K_4Sn_2Se_6$ and $K_4Sn_2Se_6$ in the presence of K_2PtCl_4 in FM. Determination of Porod's constants for $C_{18}PyPt\_Ge_2Se_6$ and $(NH_4)Pt\_Ge_2Se_6$. This material is available free of charge via the Internet at http://pubs.acs.org.

JA800741H